

This item is the archived peer-reviewed author-version of:

Long-range orientation and atomic attachment of nanocrystals in 2D honeycomb superlattices

Reference:

Boneschanscher M.P., Evers W.H., Geuchies J.J., Altantzis Thomas, Goris Bart, van Tendeloo Gustaaf, Bals Sara, et al.- *Long-range orientation and atomic attachment of nanocrystals in 2D honeycomb superlattices*

Science / American Association for the Advancement of Science - ISSN 0036-8075 - 344:6190(2014), p. 1377-1380

DOI: <http://dx.doi.org/doi:10.1126/science.1252642>

Handle: <http://hdl.handle.net/10067/1170950151162165141>

Title: Long-Range Orientation and Atomic Attachment of Nanocrystals in 2D Honeycomb Superlattices

Authors: M.P. Boneschanscher¹, W.H. Evers^{2,3}, J.J. Geuchies¹, T. Altantzis⁴, B. Goris⁴, F.T. Rabouw¹, S.A.P. van Rossum¹, H.S.J. van der Zant³, L.D.A. Siebbeles², G. van Tendeloo⁴, I. Swart¹, J. Hilhorst⁵, A.V. Petukhov¹, S. Bals⁴, and D. Vanmaekelbergh^{1,*}

Affiliations:

¹Debye Institute for Nanomaterials Science, University of Utrecht.

²Opto-electronic Materials Section, Delft University of Technology.

³Kavli Institute of Nanoscience, Delft University of Technology.

⁴EMAT, University of Antwerp.

⁵ESRF, Grenoble, Beamline ID01.

*Correspondence to: d.vanmaekelbergh@uu.nl.

Abstract: Oriented attachment of synthetic semiconductor nanocrystals is emerging as a route for obtaining new semiconductors that can have Dirac-type electronic bands like graphene, but also strong spin-orbit coupling. The two-dimensional assembly geometry will require both atomic coherence and long-range periodicity of the superlattices. We show how the interfacial self-assembly and oriented attachment of nanocrystals results in two-dimensional (2D) metal chalcogenide semiconductors with a honeycomb superlattice. We present an extensive atomic and nanoscale characterization of these systems using direct imaging and wave scattering methods. The honeycomb superlattices are atomically coherent, and have an octahedral symmetry that is buckled; the nanocrystals occupy two parallel planes. Considerable necking and large-scale atomic motion occurred during the attachment process.

Main Text: In oriented attachment a single nanocrystal (NC) is formed from two adjacent NCs through atomically matched bond formation between two specific facets. Controlled oriented attachment is currently emerging as a route to form extended one- and two-dimensional single-crystalline semiconductors of II-VI and IV-VI compounds (1–5). These superlattices are of interest in optoelectronics. Truncated nanocubes of the Pb-chalcogenide family (Fig. S1) have been recently used to create 2D atomically coherent ultrathin quantum wells (4) as well as superlattices with square or honeycomb geometries (5) (Fig. S2). The formation of such systems is remarkable given that several demanding conditions must be fulfilled. The NC building blocks must be nearly monodisperse in size and shape, and attachment should only occur with a geometrically defined subset of NC facets. The long-range atomic and nanoscale order in such systems is far from understood. For extended, atomically coherent PbSe superlattices with honeycomb geometry, immediate questions emerge on the large-scale crystallographic orientation of the NCs, the role of surface passivation of specific facets, and the atomic mechanism of attachment.

Here we report on the atomic and nanoscale analysis of atomically coherent PbSe, PbS, and CdSe honeycomb superlattices. Using HAADF-STEM tomography, we show that the honeycomb structures are buckled, i.e., the NCs occupy two parallel planes, and hence show nanoscale analogy with the proposed atomic silicene honeycomb structure. The specific orientation of the NCs in the 2D superlattice extends over hundreds of unit cells, suggesting that such types of single crystals must be formed from a pre-ordered state, e.g., at the suspension/air interface. The NCs in the honeycomb structure are considerably elongated in the direction of the NC-NC bond compared to the native building blocks. This finding points to bond formation via necking accompanied with a gradual release of the capping molecules and considerable atomic motion within the NCs. Moreover, the 2D honeycomb structures of PbSe with a rocksalt atomic lattice were robust enough to be transformed into 2D CdSe lattices with a zinc blende atomic lattice by cation-exchange and keep the nanoscale honeycomb geometry intact. This method opens a route to a new class of 2D semiconductors with tunable composition. In these structures, the nanoscale honeycomb geometry has been predicted to result in both valence and conduction bands that can be filled with Dirac-type charge carriers as in graphene, but unlike graphene, with strong spin-orbit coupling (6).

The PbSe NCs have the shape of a cantellated cube, approaching that of a rhombicuboctahedron (Fig. S1), implying that the NCs are terminated with $\{100\}$, $\{110\}$, and $\{111\}$ facets. We estimated the NC size from the radially averaged diameter of the TEM projections for >1000 particles (5.3 ± 0.4 nm) (Fig. S3). The oriented attachment of these NCs resulted in structures with long range periodicity, as visualized by means of an equilateral triangle spanning the same number of unit cells along each vertex in the HAADF-STEM image (Fig. 1A). Zooming in on the honeycomb structure (Fig. 1B) reveals that the $\langle 111 \rangle$ axes of the NCs are perpendicular to the substrate, and that the NC-NC bonds are perpendicular to three of the $\langle 110 \rangle$ axes (for a discussion on atomic contrast in HAADF-STEM images see Fig. S4). This result is also corroborated by electron diffraction (ED) patterns (Fig. 1C). The structures have a high degree of crystallinity, as observed by the occurrence of sharp spots in ED patterns recorded on selected areas with a diameter of 200 nm [Fig. 1C, for a full analysis of all peaks in the diffraction pattern see supplementary online material (Fig. S5, Table S1, S2) (7)]

There are three different models for attachment of the NCs that result in a honeycomb structure with the nanocrystal $\langle 111 \rangle$ axes perpendicular to the substrate, being attachment via the $\{110\}$, $\{111\}$, or $\{100\}$ facets, respectively (Fig. 1, D to I). The three structures appear similar from the top, but have a very different 3D geometry. Attachment via $\{110\}$ facets results in a planar, trigonal structure with bond angles between the NCs of 120° (Fig. 1, D and E). If the NCs attach via the $\{111\}$ facets the overall structure of the superlattice is slightly buckled, with a tetrahedral symmetry and NC bond angles of 109.5° (Fig 1, F and G). Attachment via $\{100\}$ facets results in a highly buckled geometry, with an octahedral symmetry and NC bond angles of 90° (Fig. 1, H and I). We used various imaging techniques to show that the experimental structure is of the octahedral type, but that the bond lengths are longer than expected on basis of a simple block model.

In the trigonal model, the attachment takes place via the $\{110\}$ facets, meaning that the $\langle 110 \rangle$ axes are parallel to the NC bonds. However, both the high-resolution HAADF-STEM images and the ED patterns show that, in our experiment, the $\langle 110 \rangle$ axes are perpendicular to the NC bonds (Fig. 1, B and C), so we could discard the trigonal model. In the buckling of the honeycomb, the HAADF-STEM images showed additional scattering strength on the NC bonds, indicating a larger than average thickness of the sample at that position. In this respect, both the tetrahedral and octahedral model are buckled and have three of the $\langle 110 \rangle$ NC axes perpendicular to the NC bonds, so it was impossible to discriminate between these remaining models by ED or 2D projections from high-resolution HAADF-STEM. Thus, we need to use a combination of scanning tunneling microscopy (STM), grazing-incidence small-angle x-ray scattering (GISAXS), and electron tomography to fully resolve the honeycomb structure.

The STM measurements showed that the honeycomb structure is indeed buckled (Fig. 2, A and B). However, topography in STM is a complicated convolution of NC height and tip radius (Fig. S6), so no quantitative height data could be extracted. We cannot measure bond lengths and angles directly in STM, but we could reliably determine the distance between next-nearest neighbors (NNN) at the same height (8.5 ± 0.8 nm, for >500 measurements). From GISAXS (Fig. 2, C and D, S7), we observed scattering peaks arising from the hexagonal order of the holes in the honeycomb structure with relative positions of $1:\sqrt{3}:2:\sqrt{7}$, as expected from a honeycomb structure (Fig. 2, C and D). Looking at the absolute peak positions in Fig. 2D, we found a hole-hole distance of 8.5 nm, in accordance with the NNN distances observed in STM. Assuming perfect honeycomb models, this distance implies a bond length of 5.2 nm for the tetrahedral and 6.0 nm for the octahedral honeycomb structure.

Figure 3 shows the tomographic reconstruction of a PbSe honeycomb structure obtained by electron tomography (Movie S1) (7–10). Slices through the reconstruction in the direction perpendicular to the substrate indicate that the two inequivalent NCs in the honeycomb unit cell are located on different heights (Fig. 3B,C) (11). We performed automated particle detection (7) on the region of interest indicated in Fig. 3D. We remark that the effect of the missing wedge in our tomography data results in a blurring of the contrast along the z -direction. In the supporting online material (7), we used simulated tomography data to show that the missing wedge in this case does not impede objective particle detection (Fig. S8). From the resulting coordinates, we constructed a model resembling the tomographic reconstruction (Fig. 3E). Using a Voronoi method, we could measure important parameters like bond angle, bond length, and NNN bond length (Fig. 3, F to H).

The obtained bond angle of $95^\circ \pm 5^\circ$ (Fig. 3F) shows that the honeycomb structure is of the octahedral type, with bonds between the $\{100\}$ facets. We can compare the ratio between bond length (6.0 ± 0.5 nm) and NNN bond length (8.9 ± 0.6 nm) that we find with the theoretical values for the different structures – for the octahedral type one would expect $1:\sqrt{2}$, for the tetrahedral type $1:\sqrt{(8/3)}$, and for the trigonal type $1:\sqrt{3}$. The ratio we find here (1:1.48) is a bit higher than the expected ratio for an octahedral structure, in agreement with the bond angles being slightly higher than 90° . The same measurement on a tomogram of a CdSe honeycomb structure shows bond angles of $85^\circ \pm 6^\circ$, slightly lower than expected (Fig. S9, S10, Movie S2).

We now have established that the NCs attach via the {100} facets into a honeycomb structure with octahedral symmetry (Fig. 1, H and I). Now we return to the bond lengths of the honeycomb structure, as extracted from TEM (Fig. S11), STM, GISAXS, and tomography. All four techniques give an independent measure of 6.0 nm for the NC bond lengths, an increase of 13% of the original NC diameter. The increased bond lengths shed light on the microscopic mechanism of facet-to-facet atomic attachment. Li et al (12) showed that, in the process of oriented attachment, the NCs are continuously rotating and moving in close proximity by means of Brownian motion to find an optimum configuration before enduring attachment takes place. We propose that, during the rotation and Brownian motion as described by Li et al (12), atomic-scale necking took place as a first step in the attachment. After necking had started, the capping molecules that remain bound to the facet were gradually removed, and the neck extended perpendicular to the bond axis by large-scale atomic motion. For PbSe NCs, considerable atomic reconfigurations have been reported (13, 14). The necking explains the elongation of the bond lengths, which also results in a considerably more open honeycomb structure than can be obtained from geometric attachment of rigid block models (compare Fig. 1H with the real structures in Fig. 1,3 and 4). In the mechanism that we propose, not all of the capping molecules have to be released at once from a facet, resulting in pathways with lower activation energy. We note that oriented attachment accompanied with neck formation is reported before as a pathway for the growth of various metal nanoparticles (15, 16).

Since the emergence of graphene (17), there is a general interest in the properties of electrons confined in a honeycomb lattice (18–23). We show that oriented attachment can form the basis of a generally applicable two-step method for the preparation of 2D semiconductors with nanoscale honeycomb geometry: assembly and oriented attachment of Pb-chalcogenide NCs with truncated cubic shape, followed by cation exchange. This is important because it has been predicted that honeycomb semiconductors of zinc blende compounds (such as CdSe) show a truly new electronic band structure, with a valence hole Dirac band and one or two conduction electron Dirac bands combined with strong spin-orbit coupling (6). We transformed PbSe honeycomb structures into CdSe superlattices via a cation exchange reaction (24, 25), and showed that honeycomb structures can also be prepared from PbS NCs (Fig. S12, S13).

Figure 4 presents the successful exchange of a PbSe honeycomb lattice into a CdSe honeycomb. The complete transformation of the PbSe lattice into CdSe is confirmed by means of energy-dispersive x-ray spectroscopy (Fig. S14). HAADF-STEM and ED measurements show that the orientation of the Se anion lattice with respect to the honeycomb periodicity is preserved (Fig. 4, A to C). This result is in agreement with earlier described mechanisms where the anion lattice is preserved during cation exchange (26, 27), and is corroborated by high-resolution HAADF-STEM measurements of honeycomb structures at intermediate stages of cation exchange (7).

References and Notes:

1. C. Pacholski, A. Kornowski, H. Weller, Self-assembly of ZnO: from nanodots to nanorods. *Angew. Chemie Int. Ed.* **41**, 1188–1191 (2002).

2. K.-S. Cho, D. V Talapin, W. Gaschler, C. B. Murray, Designing PbSe nanowires and nanorings through oriented attachment of nanoparticles. *J. Am. Chem. Soc.* **127**, 7140–7147 (2005).
3. W. Koh, A. C. Bartnik, F. W. Wise, C. B. Murray, Synthesis of monodisperse PbSe nanorods: a case for oriented attachment. *J. Am. Chem. Soc.* **132**, 3909–3913 (2010).
4. C. Schliehe *et al.*, Ultrathin PbS sheets by two-dimensional oriented attachment. *Science* **329**, 550–553 (2010).
5. W. H. Evers *et al.*, Low-dimensional semiconductor superlattices formed by geometric control over nanocrystal attachment. *Nano Lett.* **13**, 2317–2323 (2013).
6. E. Kalesaki *et al.*, Dirac cones, topological edge states, and nontrivial flat bands in two-dimensional semiconductors with a honeycomb nanogeometry. *Phys. Rev. X* **4**, 011010 (2014).
7. Information on materials and methods is available on Science Online.
8. H. Friedrich *et al.*, Quantitative structural analysis of binary nanocrystal superlattices by electron tomography. *Nano Lett.* **9**, 2719–2724 (2009).
9. M. P. Boneschanscher *et al.*, Electron tomography resolves a novel crystal structure in a binary nanocrystal superlattice. *Nano Lett.* **13**, 1312–1316 (2013).
10. P. A. Midgley, M. Weyland, 3D electron microscopy in the physical sciences: the development of Z-contrast and EFTEM tomography, *Ultramicroscopy* **96**, 413–431 (2003).
11. We would like to note here that the PbSe honeycombs suffer from beam damage, making it hard to obtain high quality tomographic reconstructions. CdSe on the other hand is more stable under the electron beam, resulting in higher quality tomographic reconstructions (compare e.g., Fig. 3 and Fig. S9 that are obtained under the same imaging conditions).
12. D. Li *et al.*, Direction-specific interactions control crystal growth by oriented attachment. *Science* **336**, 1014–1018 (2012).
13. M. A. van Huis *et al.*, Low-temperature nanocrystal unification through rotations and relaxations probed by in situ transmission electron microscopy. *Nano Lett.* **8**, 3959–3963 (2008).
14. M. A. van Huis *et al.*, Atomic imaging of phase transitions and morphology transformations in nanocrystals. *Adv. Mater.* **21**, 4992–4995 (2009).
15. J. M. Yuk *et al.*, High-resolution EM of colloidal nanocrystal growth using graphene liquid cells. *Science* **336**, 61–64 (2012).
16. J. M. Yuk *et al.*, In situ atomic imaging of coalescence of Au nanoparticles on graphene: rotation and grain boundary migration. *Chem. Commun.* **49**, 11479–11481 (2013).
17. A. H. Castro Neto, N. M. R. Peres, K. S. Novoselov, A. K. Geim, The electronic properties of graphene. *Rev. Mod. Phys.* **81**, 109–162 (2009).
18. K. K. Gomes, W. Mar, W. Ko, F. Guinea, H. C. Manoharan, Designer Dirac fermions and topological phases in molecular graphene. *Nature* **483**, 306–310 (2012).

19. G. De Simoni *et al.*, Delocalized-localized transition in a semiconductor two-dimensional honeycomb lattice. *Appl. Phys. Lett.* **97**, 132113 (2010).
20. M. Gibertini *et al.*, Engineering artificial graphene in a two-dimensional electron gas. *Phys. Rev. B* **79**, 241406 (2009).
21. C.-H. Park, S. G. Louie, Making massless Dirac fermions from a patterned two-dimensional electron gas. *Nano Lett.* **9**, 1793–1797 (2009).
22. C.-H. Park, L. Yang, Y.-W. Son, M. L. Cohen, S. G. Louie, New generation of massless Dirac fermions in graphene under external periodic potentials. *Phys. Rev. Lett.* **101**, 126804 (2008).
23. A. Singha *et al.*, Two-dimensional Mott-Hubbard electrons in an artificial honeycomb lattice. *Science* **332**, 1176–1179 (2011).
24. J. M. Luther, H. Zheng, B. Sadtler, A. P. Alivisatos, Synthesis of PbS nanorods and other ionic nanocrystals of complex morphology by sequential cation exchange reactions. *J. Am. Chem. Soc.* **131**, 16851–16857 (2009).
25. B. J. Beberwyck, Y. Surendranath, A. P. Alivisatos, Cation exchange: a versatile tool for nanomaterials synthesis. *J. Phys. Chem. C* **117**, 19759–19770 (2013).
26. S. Bals *et al.*, Three-dimensional atomic imaging of colloidal core-shell nanocrystals. *Nano Lett.* **11**, 3420–3424 (2011).
27. M. Casavola *et al.*, Anisotropic cation exchange in PbSe/CdSe core/shell nanocrystals of different geometry. *Chem. Mater.* **24**, 294–302 (2012).
28. J. S. Steckel, B. K. H. Yen, D. C. Oertel, M. G. Bawendi, On the mechanism of lead chalcogenide nanocrystal formation. *J. Am. Chem. Soc.* **128**, 13032–13033 (2006).
29. K. A. Abel, J. Shan, J.-C. Boyer, F. Harris, F. C. J. M. van Veggel, Highly photoluminescent PbS nanocrystals: the beneficial effect of trioctylphosphine. *Chem. Mater.* **20**, 3794–3796 (2008).

Acknowledgments: We thank the ESRF (Grenoble, France) for providing the synchrotron beamtime and the staff of ESRF beamline ID-01 for their support. We thank Carlo van Overbeek for his help on the PbS sample. This research is part of the programmes “Control over Functional Nanoparticle Solids (FNS)”, and “Designing Dirac Carriers in semiconductor honeycomb superlattices (DDC)” that are supported by the Foundation of Fundamental Research on Matter (FOM) which is part of the Dutch Research Council (NWO). The authors also acknowledge financial support from the European Research Council (ERC Advanced Grant #24691-COUNTATOMS, ERC Starting Grant #335078-COLOURATOM). The authors also appreciate financial support from the European Union under the Seventh Framework Program (Integrated Infrastructure Initiative N. 262348 European Soft Matter Infrastructure, ESMI). This work was supported by the Flemish Fund for Scientific Research (FWO Vlaanderen) through a PhD research grant to B.G.

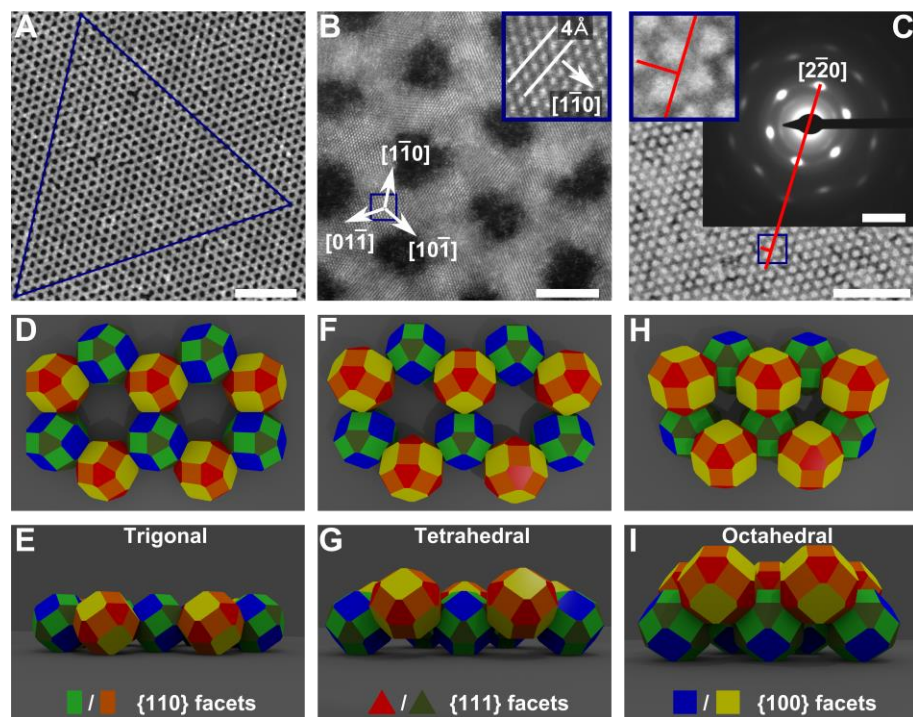


Fig. 1. Single-crystalline PbSe honeycomb structures created by oriented attachment. **(A)** HAADF-STEM image of the honeycomb structure (bright on a dark background). The equilateral triangle shows the long-range ordering of the structure. Scale bar, 50 nm. **(B)** High-resolution HAADF-STEM image showing that the $\langle 111 \rangle$ NC axes are perpendicular to the honeycomb plane, and three of the $\langle 110 \rangle$ axes are perpendicular to the NC bonds. Inset: zoom-in on the atomic columns indicated by the blue box. Scale bar, 5 nm. **(C)** Electron diffraction pattern showing the high degree of crystallinity. TEM image in the background shows the area on which the ED pattern was recorded (the honeycomb appears dark on a bright background). Red line and inset show the orientation of the diffraction spots with respect to the honeycomb structure, confirming that the $\langle 110 \rangle$ axes are perpendicular to the NC bonds. Scale bar, 50 nm (TEM), 5 nm^{-1} (ED). **(D to I)** Models of the honeycomb structure with cantellated cubes as nanocrystals. The two inequivalent sites in the honeycomb lattice are indicated by yellow/red and blue/green NCs. Rectangles (orange, light green) represent $\{110\}$ facets, triangles (red, dark green) $\{111\}$ facets, and squares (yellow, blue) $\{100\}$ facets. **(D,E)** Top and side view of the trigonal structure. **(F,G)** Top and side view of the tetrahedral structure. **(H,I)** Top and side view of the octahedral structure.

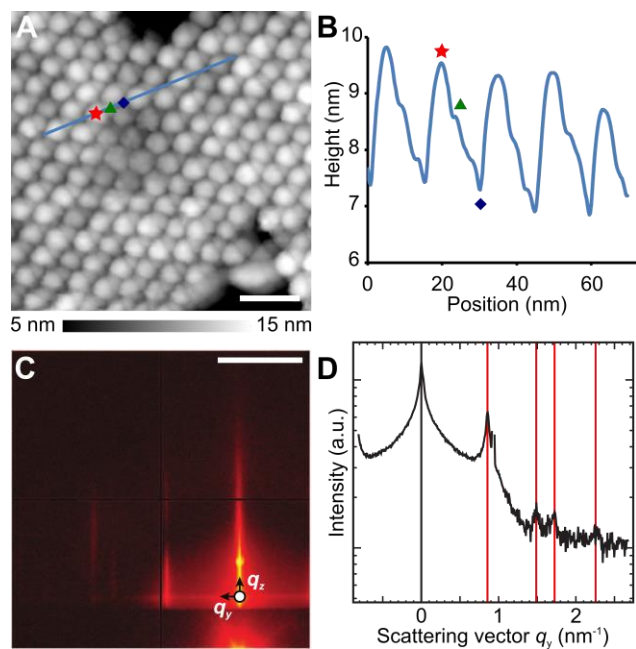


Fig. 2. STM and GISAXS measurements on the PbSe honeycomb structures. **(A)** Constant-current STM measurement showing high (red star) and low (green triangle) nanocrystals forming a honeycomb structure. Feedback settings 3.5 V and 20 pA; scale bar, 20 nm. **(B)** Height profile along the blue line indicated in **(A)**. The position of a high NC (star), low NC (triangle), and hollow site (diamond) are indicated. **(C)** GISAXS pattern of a honeycomb structure on top of a Si(100) substrate, under an angle of incidence of 0.7 degrees. Scale bar, 1 nm^{-1} . **(D)** Line trace in the horizontal direction indicated in **(C)**, revealing the in-plane order. Red lines mark diffraction peaks with relative positions of $1:\sqrt{3}:2:\sqrt{7}$, arising from the hexagonal order of the holes in the structure.

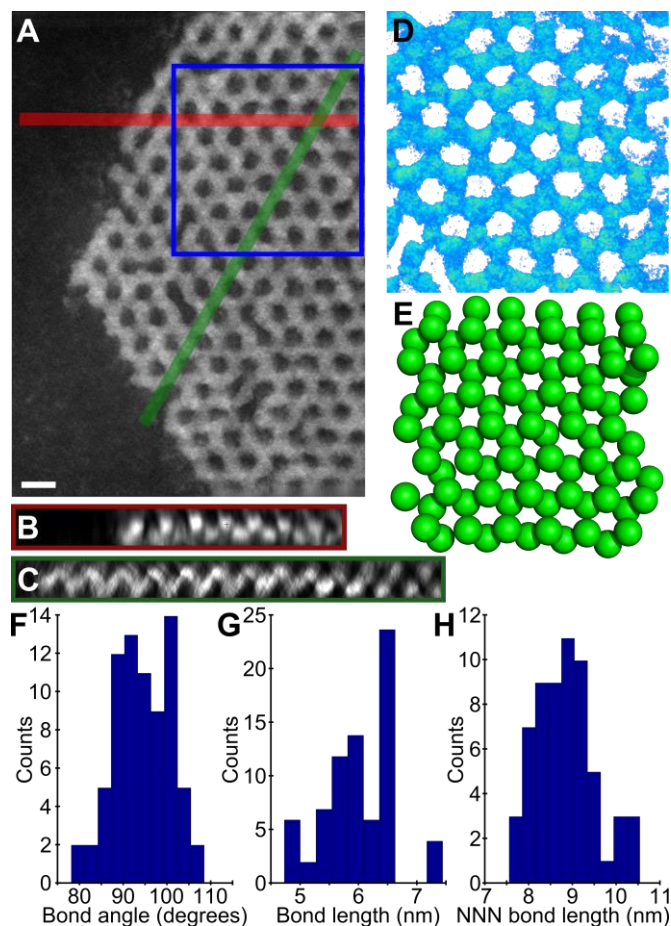


Fig. 3. HAADF-STEM tomography on a PbSe honeycomb structure. **(A)** Overview of the honeycomb structure obtained by averaging the tomographic reconstruction in the direction perpendicular to the substrate. Scale bar, 10 nm. **(B,C)** slices through the tomogram perpendicular to panel (A), along the (B) red, or (C) green line indicated in (A). **(D)** Iso-volume rendering of the tomographic reconstruction in the region indicated with the blue box in panel (A). **(E)** Equally sized spheres plotted on the coordinates obtained by automated particle detection in the region indicated in blue in panel (A). **(F)** Bond angles measured from the coordinates in (E), showing a bond angle of $95 \pm 5^\circ$. **(G)** Bond lengths to nearest neighbors, showing a bond length of 6.0 ± 0.5 nm. **(H)** Bond lengths to next-nearest neighbors, showing a NNN bond length of 8.9 ± 0.6 nm.

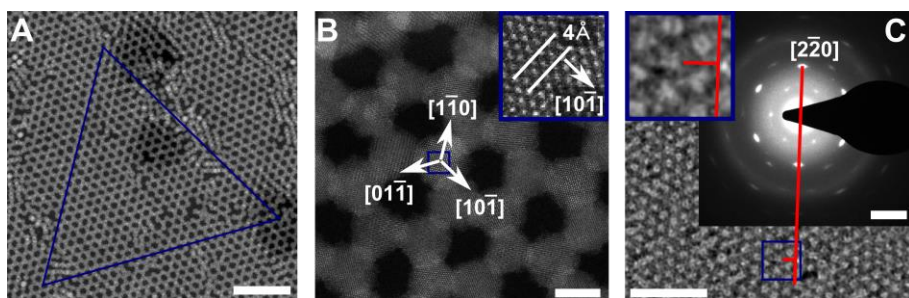


Fig. 4. Single crystalline CdSe honeycomb structures created by cation exchange. **(A)** HAADF-STEM image of the CdSe honeycomb structure. The honeycomb appears bright on a dark background. The equilateral triangle shows that the long range ordering of the structure is retained. Scale bar, 50 nm. **(B)** High-resolution HAADF-STEM image showing that the orientation of the Se anion lattice with respect to the superlattice geometry is preserved. Inset: zoom-in on the area indicated by the blue box. Scale bar, 5 nm. **(C)** An ED pattern showing that the high degree of crystallinity is preserved. TEM image in the background shows the area on which the ED pattern was recorded (the honeycomb appears dark on a bright background). Red line and inset show the orientation of the diffraction spots with respect to honeycomb structure, confirming that the $\langle 110 \rangle$ axes are perpendicular to the NC bonds. Scale bar, 50 nm (TEM), 5 nm⁻¹ (ED).

Supplementary Materials

www.sciencemag.org
 Materials and Methods
 Figs. S1 to S14
 Tables S1 to S2
 References (28,29)
 Movies S1 to S2